Evaluation and modeling of mechanical behaviors of thermosetting polymer under monotonic and cyclic tensile tests

Evaluation and modeling of mechanical behaviors of thermosetting polymer under monotonic and cyclic tensile tests

Makoto Uchida, Ryohei Wakuda, Yoshihisa Kaneko

UCHIDA, M., WAKUDA, R., & KANEKO, Y. (2019). Evaluation and modeling of mechanical behaviors of thermosetting polymer under monotonic and cyclic tensile tests. *Polymer*. 174, 130-142.

Evaluation and modeling of mechanical behaviors of thermosetting polymer under monotonic and cyclic tensile tests

Makoto Uchida, Ryohei Wakuda and Yoshihisa Kaneko

Abstract

A nonlinear elastic-inelastic model for a thermosetting polymer is proposed based on the molecular chain network theory. In the proposed model, the bond of the polymer chain is divided into physical and chemical bonds, and the physical bond is allowed to separate and recombine during the deformation. The decrease in the rigidity and increase in the inelastic strain are related to the development of the physical bond density to represent the characteristic deformation behavior of the polymer. A rate-form large deformation constitutive equation is then formulated based on the updated Lagrangian method. Additionally, deformation behaviors of the epoxy under monotonic and cyclic tensile tests were evaluated by experimental and computational studies. The experimental results of the monotonic tensile test displayed a gradual transition from elastic to inelastic deformation, strain softening behavior after the macroscopic yielding stress, and an increase in the initial slope and the macroscopic yielding stresses with an increasing strain rate. The computational model can represent such characteristics by controlling the development of the physical bond density. In a cyclic test, a decrease in the rigidity and an increase in the residual strain with increasing cycles were observed even in a small strain range. Such inelastic deformation depended on the strain rate and the given upper stress in the cyclic test. Further, the proposed model successfully reproduced such nonlinear behavior in the cyclic test.

Keywords: Thermosetting polymer, Constitutive equation, Elasto-viscoplastic deformation, Cyclic test, Molecular chain network theory

1. Introduction

Fiber-reinforced polymer (FRP) is widely employed in industrial structures as an alternative material to metal. To advance the mechanical performance of FRP further, many active studies have been conducted: exploring new reinforcement fibers [1, 2], improving the interface/interphase [3], and optimizing the fiber distribution [4]. Furthermore, mechanical models based on the anisotropic constitutive equation [5, 6], micromechanical modeling [7], and a multiscale model by the homogenization method [8, 9] have been proposed for predicting the deformation behavior of FRP. In these studies, a simple elastic or viscoelastic model was employed to describe the deformation behavior of the polymer matrix. The polymer matrix employed in the FRP is a thermosetting or thermoplastic polymer. These polymers exhibit a nonlinear mechanical response, depending on the strain rate and temperature, even under a small strain range. When long-term loadings are applied to

FRP, such as cyclic and creep loading, an inelastic strain is accumulated in the polymer matrix. Therefore, to predict the time-dependent mechanical performance of the material, creating an accurate nonlinear mechanical model for the polymer matrix is a very important task.

There are many types of polymer, and their mechanical properties are different depending on the type polymer. The deformation behavior of a polymer is often described based on the kinetics of the network of the molecular chain. This framework is referred to as the molecular chain network theory. Note that the molecular chain referred to here is a sectional part of a polymer chain between two crosslinks. One of the important parameters that characterizes the mechanical properties of a polymer is the glass transition temperature T_g. A polymer with a temperature above T_g is in the rubbery state, which exhibits entropic elasticity. In this state, the intermolecular force acting on the molecular chain is relatively small, and the molecular chain deforms by the force acting on both ends.

Arruda and Boyce [10] proposed the well-known eight-chain model to reproduce the three-dimensional deformation behavior of rubber based on non-Gaussian statistics [11]. Edward and Vilgis proposed a rubber elasticity model in which a conformation entropy function for the entangled polymer was introduced [12]. The polymer network employed in this model is formed by permanent crosslinks (covalent bonds) and additional entanglements that behave like a slip-link. The concept of this model, which is referred to as the "EV model" hereafter, was employed to reproduce the time-dependent mechanical behavior of a glassy polymer near T_g [13, 14].

The mechanical properties of a polymer at temperatures below T_g are quite different from those in the rubbery state. The strength of the polymer increases considerably because the movement of the molecular chain is constrained by the intermolecular force. Especially in the earlier stage of the deformation, the polymer exhibits an energetic elasticity similar to that of a metal. Boyce et al. [15] determined the resistance to this inelastic deformation of a glassy polymer into resistances based on the rotation and orientation of the molecular chain. The former was introduced to evaluate the plastic flow from the initial to middle range of deformation using the double-kink model proposed by Argon [16]. In this model, the pressure dependency and true strain softening are reproduced by controlling the shear strength. The latter is introduced as the back stress to the plastic deformation in the form of a non-Gaussian statistical model. This latter idea of the orientation of the molecular chain has been widely employed to represent the hardening in the large strain range of the glassy polymer, whereas several kinds of alternative models were proposed to represent the response from the initial to middle strain range.

Hassan et al. [17, 18] reproduced the gradual elastic-plastic transition in the earlier strain range and the following softening process of the glassy polymer by introducing the development of a local free volume in the polymer. In this model, local yielding occurs prior to macroscopic yielding at the relatively weak sites (the high free-volume sites), which results in a gradual elastic-plastic transition. The new weak sites develop with increasing deformation, and this induces softening of the material in

the plastic flow. On the other hand, Tomita and Uchida [19] performed a finite element method (FEM) simulation of the deformation behavior of a glassy polymer having a heterogeneously distributed local strength. They also demonstrated that local yielding in the weaker sites induces the gradual elastic-plastic transition, whereas the softening that follows is suppressed owing to the preferential orientation hardening at the initially yielding site.

The inelastic model employed in the above studies were related to the deformation of the molecular chain. In addition, inelastic models based on the relative displacement between chains were proposed. Anand et al. [20], Srivastava et al. [21], and Bouvard et al. [22] proposed thermomechanical models and reproduced the time-dependent behavior of glassy polymers in various temperature ranges. In these models, the plastic flow accompanied by the true strain softening was described by the slippage of physically bonded molecular chains, which were observed in a molecular dynamics simulation [22]. Gehring et al. added the weaker bonds (such as van der Walls and H-bonds) into the EV model to simulate the time dependent behavior of polyethylene terephthalate [23].

Inelastic deformation in the crystalline phase of a semi-crystalline polymer (SCP), in which molecular chains are uniformly arranged by the intermolecular force, also occurs owing to the relative displacement between chains. Because the intermolecular force of the chain is much smaller than the intramolecular force, slip deformation along the molecular chain occurs. This inelastic deformation based on the slip is often modeled by the crystalline plasticity theory [24], which is widely employed for metal materials. Because an amorphous region remains between the crystalline regions in the microstructure of the SCP, the SCP can be regarded as a composite material of the crystalline and amorphous phases [25-27]. Furthermore, a characteristic mesoscopic structure called spherulite is formed during solidification of the SCP. Therefore, a complex multiscale model is required to capture the micro- to macroscopic deformation behavior of the SCP [26, 27].

Uchida and Tada [27] proposed a three-scale mechanical model using a laminar composite model and FEM-based homogenization method. The elasto-viscoplastic deformation behavior of high-density polyethylene under several macroscopic boundary conditions was numerically investigated. Although the proposed model successfully represented the development of the microstructure and the macroscopically averaged mechanical response, the onset and propagation of macroscopic necking during a uniaxial tensile test [28] could not be predicted. The growth of macroscopic necking relates to the degree of softening after macroscopic yielding. To represent such a nonuniform macroscopic deformation, the collapse and rearrangement of the crystal structure, (in other words, the decomposition and recombination of the bonding by the intermolecular force between molecular chains) should be introduced in the model.

The above models were mainly proposed to demonstrate the inelastic deformation behavior of thermoplastic polymer. On the other hand, mechanical model of the thermosetting polymers based on the polymer network is also very important in predicting the mechanical performance of those

composite. In particular, the modeling of the time-dependent deformation behavior of very small strain range is very important for thermosetting polymers since the application of them is mostly limited to a small strain range. A three-dimensional crosslink network is constructed in the thermosetting polymer, which increases the strength of the material. Although the thermosetting polymer also deforms in a large strain range when the environmental temperature is close to T_g [29], the representative thermosetting polymer (such as epoxy, phenol resin, or melamine), usually exhibits brittle behavior at room temperature. However, both thermosetting and thermoplastic polymers exhibit nonlinear viscoelastic deformation behavior, even in a very small strain range, and complex mechanical behavior such as ratcheting was observed under cyclic loading [30-32]. This irreversible response for the cyclic test indicates that the material microstructure has changed during the loading and unloading process even in small stress level. The separation and recombination of the physical bonds are one of the possible factors to induce such the microstructure change. Therefore, although the chemical bonding is important to discuss the strength of the thermosetting polymer, the physical bonding is also important especially to predict the nonlinear behavior in the small stress levels.

The main purpose of this study is to establish a mechanical model to reproduce the time-dependent nonlinear behaviors from small to large strain range. Usually, a more complex mechanical model is required to predict complex and long-term loading conditions such as loading/unloading, cyclic loading, creep, and stress relaxation. Mechanical models to predict the deformation behavior under complex and long-term loading conditions were proposed for SCP [33], polypropylene [34], Ultra High Molecular Weight Polyethylene [35] and epoxy [36]. In these models, a rheological approach employing the multiple components of springs and dashpots was introduced to reproduce the experimental results. On the other hand, the micromechanical model based on the kinetics of the molecular chain explained in the above paragraphs was not applied in these studies. The modeling of deformation behavior in such a complex loading condition (based on the framework of the molecular chain network theory) helps to further knowledge of microstructure development.

In the present study, a mechanical model that can predict the deformation behavior under monotonic and cyclic loadings for a thermosetting polymer below T_g is constructed, based on the molecular chain network theory. The main idea of this study is that the bond of the molecular chain is divided into chemical and physical bonds that correspond to covalent bonds and bonds by intermolecular force, respectively. In addition, the density of the physical bond is assumed to change during the deformation owing to the separation and recombination of the bond. The slippage of physical bonds in a glassy polymer and the collapse and rearrangement of the crystalline structure in SCP can be recognized as representative cases of the deformation mechanisms relating to the development of the physical bond. First, the mechanical responses of monotonic and cyclic tensile tests for low-viscosity epoxy resin ware experimentally evaluated. Subsequently, a mechanical model based on the molecular chain network theory is established to predict the obtained results.

2. Experiment

2.1 Experimental method

Epoxy is widely employed as the polymer matrix of fiber-reinforced polymer. Monotonic and cyclic tensile tests of an epoxy specimen were performed in this study. The epoxy used in the experiment is a commercial low-viscosity epoxy resin (Z-1, Nissin Resin Co., Ltd.). The tensile specimen shown in Fig. 1 was formed using a silicone mold. Stainless-steel specimens with the same shape were first machined, and then they were used to make a silicone mold. Subsequently, a mixture of the main and curing agents, which was mixed and degassed using a planetary centrifugal mixer (AR310, Thinky Corp.), was poured into the mold. The mixing and degassing conditions were 1000 rpm for 1 min and 1400 rpm for 1 min, respectively. Subsequently, the specimens were obtained by curing at room temperature for 24 h. Because the free surface of the specimen bulged owing to surface tension, the surface was mechanically polished using abrasive paper (grades 150 and 400).

The stress-strain response until fracture was evaluated by a monotonic tensile test. The tensile tests were performed using a compact tensile & compression tester (IMC-18E0, Imoto Machinery Co., Ltd.) under different strain rates of $\dot{E}_{22} = 3\times10^{-5}$, 1×10^{-4}, and 3×10^{-4}/s at room temperature. To evaluate the nonuniform deformation in the large strain range of the monotonic tensile test quantitatively, the tensile strain was measured by the digital image correlation (DIC) method. Here, netDIC [28], which enables accurate and stable measurement of the strain distribution on the specimen surface even under large and/or nonuniform deformation, was employed to measure the comparatively large strain and the strain concentration prior to the fracture. A random speckle pattern was created on the specimen surface by a spray, and sequential images of the surface were captured using a digital single-lens reflex camera (body: K20, Pentax Co., Ltd.; lens: DFA Macro 50 mm F2.8, Pentax Co., Ltd.).

The distribution of the true strain tensor can be evaluated by the development of the velocity field on the specimen surface with reference and current coordinates $\boldsymbol{X}$ and $\boldsymbol{x}$. First, a triangular element was constructed using the velocity-measured points $P^{(1)}$, $P^{(2)}$, and $P^{(3)}$. The two-dimensional components of the velocity gradient $\boldsymbol{L} = \partial \boldsymbol{v}/\partial \boldsymbol{x}$ of the triangular elements were then evaluated using the velocity-velocity gradient translation matrix similar to that in the usual FEM procedure. The deformation gradient $\boldsymbol{F}$ was updated using the obtained $\boldsymbol{L}$ as

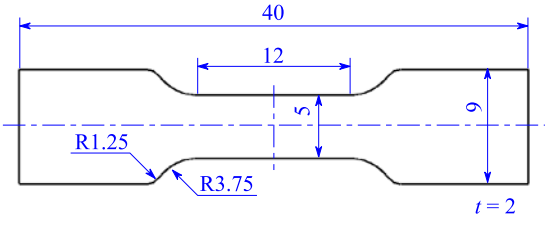

Fig. 1 Shape of tensile specimen (in mm).

$$\boldsymbol{F}\left(t+\Delta t\right)=\left(\boldsymbol{I}+\boldsymbol{L}\Delta t\right)\cdot\boldsymbol{F}\left(t\right), \tag{1}$$

where $\boldsymbol{I}$ is the unit tensor. The left Cauchy-Green deformation tensor $\boldsymbol{A}$ was then given by

$$\boldsymbol{A}=\boldsymbol{F}\cdot\boldsymbol{F}^{T}. \tag{2}$$

Thus, the local true strain tensor was calculated as

$$\boldsymbol{\varepsilon}=\ln\left(\boldsymbol{A}^{1/2}\right). \tag{3}$$

In the tensile test, uniaxial tension in the X_2 direction was given to the specimen. Therefore, the global true strain $\bar{\varepsilon}_{22}$ and global true stress $\bar{\sigma}_{22}$ in the tensile direction were evaluated as

$$\bar{\varepsilon}_{22}=\frac{1}{V}\int_V \varepsilon_{22}dV, \tag{4}$$

$$\bar{\sigma}_{22}=\frac{F}{A_0}\exp\left(\bar{\varepsilon}_{22}\right), \tag{5}$$

where V is he volume of the displacement evaluation region, F is the tensile load, and A_0 is the initial cross section of the specimen.

Cyclic tensile tests were also performed using the same testing machine at room temperature. In this test, the crosshead speed was kept constant, and the movement direction was reversed when the loading reached the predetermined values. Three upper stresses of 5, 10, and 15 MPa were used in the cyclic tests whereas the lower stress was fixed at 0.5 MPa. These upper stresses were much smaller than the macroscopic yielding stress confirmed in the monotonic tensile test. Note that the maximum stress before the true strain softening is referred to as the macroscopic yielding stress, as a barometer to characterize the mechanical properties of the material. Therefore, the macroscopic yielding stress does not correspond to the stress distinguishing the elastic and inelastic deformation in this study. To evaluate the strain rate in the cyclic tests, two strain rates of $\dot{E}_{22}=3\times10^{-5}$ and 3×10^{-4}/s were given to the specimen. A total of 100 loading-unloading cycles were given to the specimen for all test conditions. Because the deformation was almost uniform in a small strain range, a strain gage (KFEL-5-120- C1, Kyowa Electronic Instruments Co., Ltd.) was used to measure the tensile strain in the cyclic tests.

2.2 Experimental results

The experimental results for the monotonic and cyclic tensile tests are presented in this section. Fig. 2 shows the relationships between the true stress and strain obtained from the monotonic tensile tests at different crosshead speeds. The average true strain was estimated using the velocity field measured by netDIC. Although the stress increased almost linearly in the initial stage of the tensile deformation, the slope of the response continued to decrease until it reached a negative value. The initial slope and macroscopic yielding stress increased with the crosshead speed because of the

viscosity of the material. The macroscopic yielding stresses for the tensile tests with $\dot{E}_{22} = 3\times10^{-4}$ and 3×10^{-5} /s were approximately 50 and 35 MPa, respectively. In the tests with a larger strain rate, the specimen fractured immediately after the response showed macroscopic yielding whereas a relatively large deformation was observed in the test with a smaller strain rate.

The distributions of the strain in the loading direction at different stages of deformation (a) to

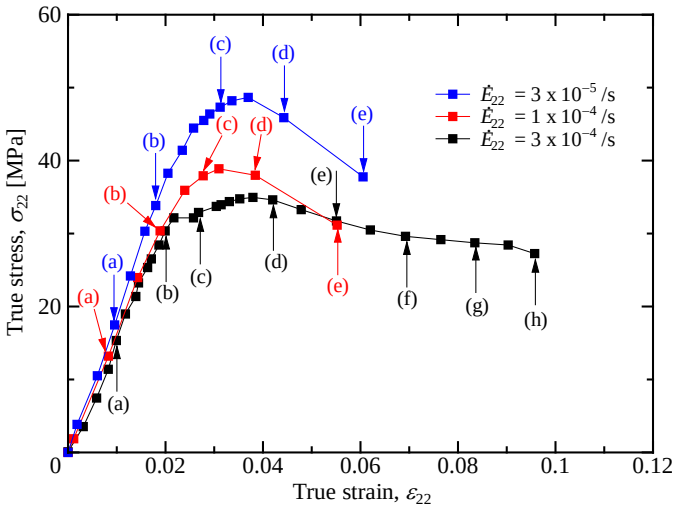

Fig. 2 Relationships between true stress and true strain obtained by monotonic tensile tests with different crosshead speeds.

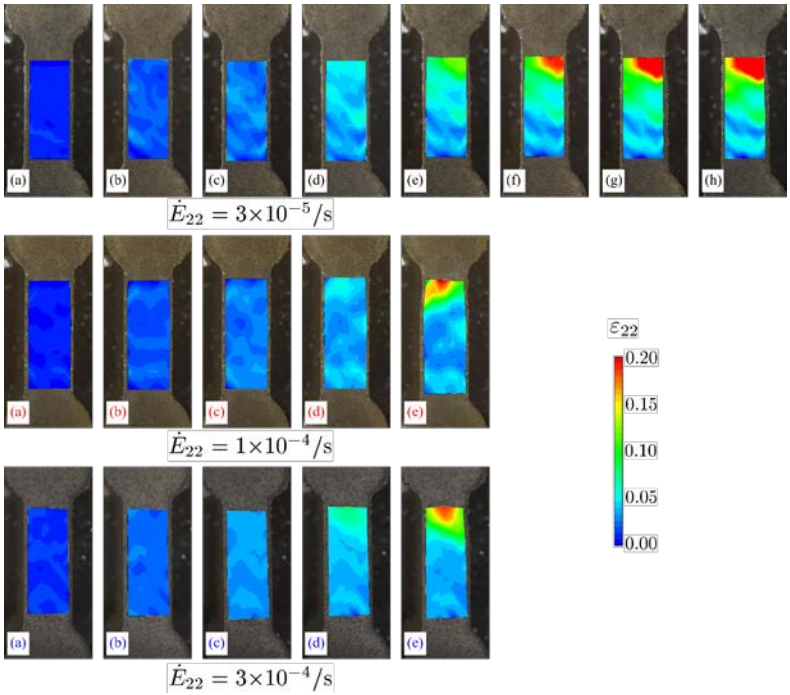

Fig. 3 Development of distribution of true strain in loading direction measured by netDIC.

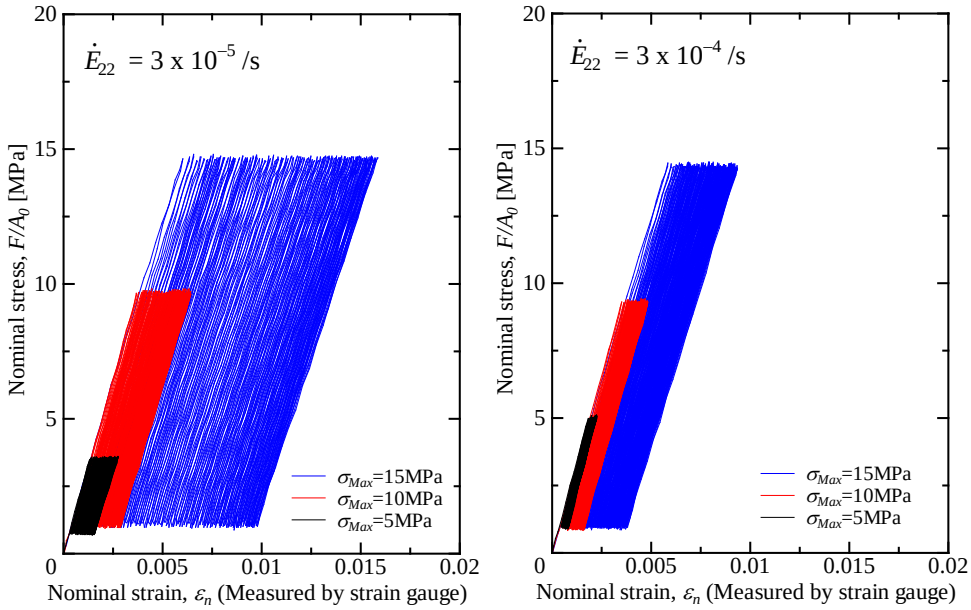

Fig. 4 Relationships between nominal stress and strain obtained from cyclic tensile tests with different maximum stresses and crosshead speeds.

(h) in Fig. 2 are shown in Fig. 3. The area in which the velocity field was measured by netDIC was the central region of the gage section of the specimen, as shown in Fig. 3. A clear strain concentration was not be observed in stages (a) to (c) for all conditions. After the true stress showed macroscopic yielding, a relatively clear strain concentration occurred in the region between the gage and grip sections, and the necking formed in this area. Although the neck propagation was often observed after the necking in the thermoplastic polymers owing to the orientation hardening of the molecular chain, the epoxy specimen fractured immediately after the neck was formed.

The relationships between the nominal stress and strain in cyclic tensile tests with different upper stresses and crosshead speeds are shown in Fig. 4. A nonlinear response and residual strain were observed for all conditions, even though the regions of the cyclic stress were much smaller than the macroscopic yielding stress observed in the monotonic tensile test. The result of increasing the residual strain with an increase in the upper stress and decrease in the crosshead speed indicated that the creep of the material is an important behavior that determines the residual strain in the cyclic test.

The obtained experimental results clarified the complex time-dependent behavior of the thermosetting polymer. A nonlinear mechanical model for this material is established based on the kinetics of the molecular chain in the following sections.

3 Mechanical Model

3.1 Concept of model

The nonlinear mechanical behavior of the thermosetting polymer was modeled based on the kinetics of the molecular chain. Polymeric materials above the glass transition temperature T_g are in

the rubbery state and show entropy-elasticity. To describe the deformation behavior of the rubber, the microscopically distributed polymer chains were modeled by a periodically crosslinked polymer network structure, and the deformation of the molecular chain was assumed to correspond to the deformation of the rubber. The molecular chain, which is a sectional part of a polymer chain between two crosslinks, consists of multiple segments. Arruda and Boyce proposed an eight-chain model [10] to reproduce the three-dimensional nonlinear mechanical response of rubber based on non-Gaussian statistics [11] as

$$\boldsymbol{\sigma} = \frac{1}{3} C_R \sqrt{N} \frac{\boldsymbol{A} - \lambda_c \boldsymbol{I}}{\lambda_c} \mathcal{L}^{-1}\left(\frac{\lambda_c}{\sqrt{N}}\right) + p\boldsymbol{I}\,, \tag{6}$$

where $\boldsymbol{\sigma}$ is the Cauchy stress, $C_R = nk_BT$ is the rubber elasticity, n is the density of the molecular chain, k_B is Boltzmann's constant, T is the absolute temperature, $N = N_A/n$ is the number of segment in a chain, N_A is the total number of segments per volume, $\boldsymbol{A} = \boldsymbol{F}\boldsymbol{F}^T$ is the left Cauchy-Green deformation tensor, $\lambda_c = \mathrm{tr}\boldsymbol{A}/3$ is the chain stretch, $\mathcal{L}^{-1}(x)$ is the inverse of the Langevin function $\mathcal{L}(x) = \coth x - 1/x$, and p is the pressure. The material parameters characterizing the mechanical response of the rubber are C_R and N, which are proportional and inversely proportional to chain density n, respectively. The rubber elasticity C_R affects the initial stiffness, and the square root of the segment number for a chain, $\sqrt{N}$, corresponds to the stretch limit of the material.

In the polymer below T_g, polymer chains are physically bonded by an intermolecular force (such as the van der Waals force) in addition to the chemical (covalent) bond, as shown in Fig. 5. Because this physical bond (PB) is weaker than the chemical bond (CB), separation and recombination of PB may occur owing to the external force and temperature changes. In the present study, we assume that the inelastic deformation of the polymer is caused by the separation and recombination of PB, and they are related to the development of the mechanical properties of the polymer. This strategy is similar to the approach employed in the EV model [12-14, 23], in which the polymer network is formed by permanent crosslinks and slippable entanglements. The reptation theory in the tube model [37] and the slip deformation of the molecular chain in crystalline polymer [24] are also recognized as intermolecular force-driven kinetic models for the polymer.

The deformation process of a ther mosetting polymer below T_g in the proposed model is

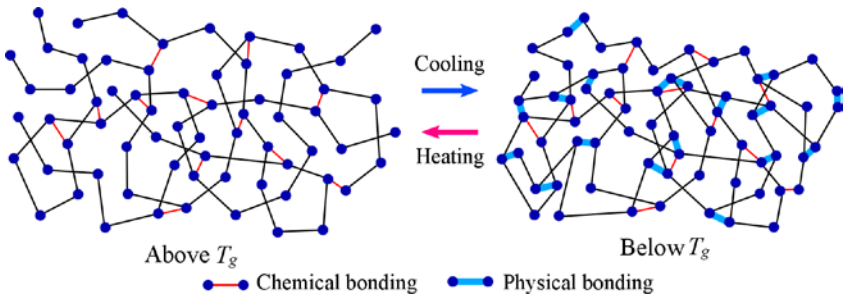

Fig. 5 Schematic illustration of polymer chain above and below glass transition temperature T_g. Polymer chain bonded chemically and physically below T_g.

schematically illustrated in Fig. 6. The deformation mechanisms in each deformation stage are explained as follows:

1. (a) to (b): Polymer chains are physically bonded at a high density. When the external load is applied to the polymer, the intermolecular force acting on the physically bonded molecular chains (PB chains) increases owing to the interaction potential energy between the chains. This force must be balanced with the internal force driving the deformation of the PB-chain.
2. (b) to (c): The intermolecular force further increases with the external load, and the PB is separated when the force becomes larger than the strength of the PB. Because the intermolecular force is not uniform for all chains in the polymer, the density of the PB decreases gradually by the continuous separation of the PBs in the polymer. As a result, the rigidity of the polymer gradually decreases.
3. (c) to (d): The separated polymer chain is physically recombined with different polymer chains in the deformed configuration. This rearrangement of the polymer network generates the inelastic deformation of the polymer. The separation and recombination of the PB induce a continuous decrease in the rigidity and an increase in the inelastic strain of the polymer, which results in true strain softening.
4. (d) to (e): With an increase in the deformation, the molecular chains orient to the elongation direction by rearranging the polymer network. This results in the elongation of the chemically bonded molecular chain (CB chain), which induces an increase in the stress in a large strain range.

The above deformation mechanisms are modeled in the next section.

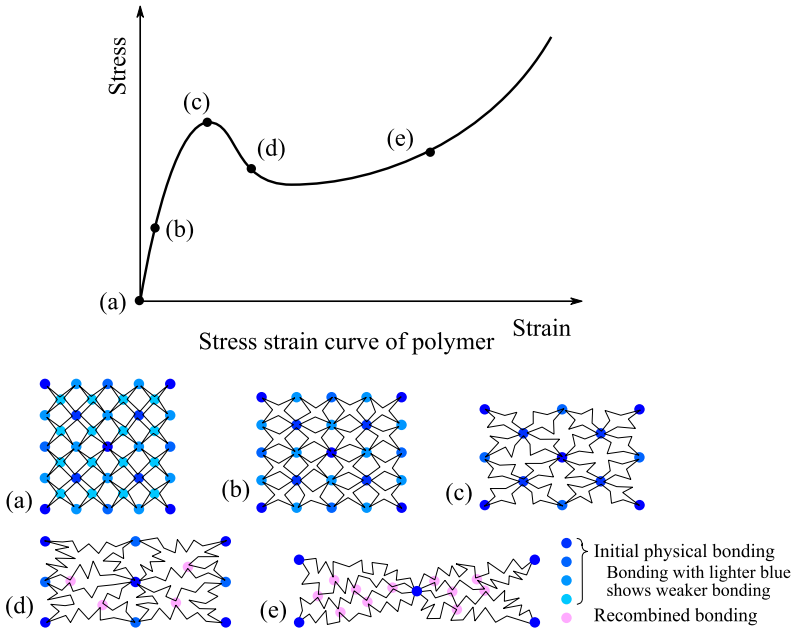

Fig. 6 Schematic images of polymer network structure at different degrees of deformation.

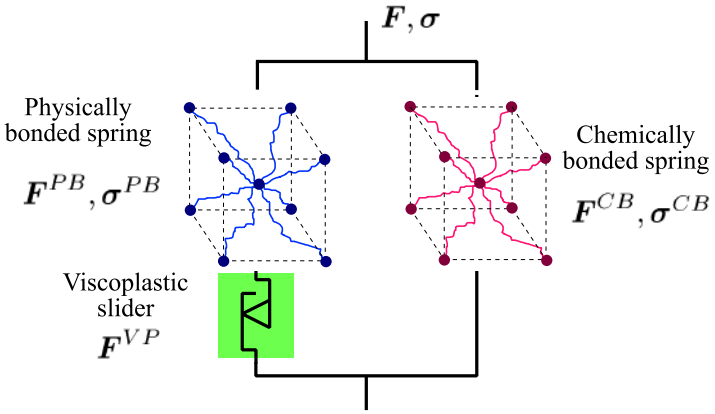

Fig. 7 Schematic illustration of proposed mechanical model constructed by physical- and chemical-bonding spring, linear spring and viscoplastic element.

3.2 Basic equations

The concrete mechanical model proposed in this study is explained next. A schematic of the employed model is shown in Fig. 7. The entire stress $\boldsymbol{\sigma}$ for the polymer is divided into that by PB and CB chains, $\boldsymbol{\sigma}^{PB}$ and $\boldsymbol{\sigma}^{CB}$, respectively. In this model, the elastic deformation in the small strain range is mainly characterized by the spring on the left side. For metal materials, the reversible deformation is based on the energy-elasticity owing to the change in the interatomic distance. On the other hand, the reversible deformation in the polymer is caused not only by change in the intermolecular distance, but also by deformation of the molecular chain. When the polymer network is tightly linked by PB in the initial state, the deformation of the molecular chain exhibits almost no deformation because the number of segments for a chain, N, close to 1. However, if N increases by the separation of PB, the molecular chain deforms based on the entropy-elasticity. Therefore, the elastic reversible deformation in small strain range is represented by a high-chain density eight-chain model with a linear elasticity model. Here, we assumed that the shear strain by energy-elasticity is much smaller than that by entropy-elasticity, only the energy-elasticity volume strain is introduced with bulk modulus of the material. A similar concept was employed in the extended EV model [23].

The stress for a PB chain $\boldsymbol{\sigma}^{PB}$ acting on the left side of the model induces the reversible elastic deformation $\boldsymbol{F}^{PB}$ in the small strain range. Furthermore, an inelastic deformation $\boldsymbol{F}^{VP}$ occurs owing to the recombination of the separated PB chain. Consequently, two deformable elements, namely, the energy- and entropy-elastic spring and viscoplastic slider, are allocated on the left side. On the other hand, an entropy-elastic spring for the CB chain is allocated on the right side of the model. This spring represents the orientation hardening of a crosslinked molecular chain in the large strain range. The eight-chain model is also employed to represent the CB chain. Hereafter, the eight-chain springs consisting of PB and CB chains are referred to as PB and CB springs, respectively.

The deformation gradient and stress of the entire system, $\boldsymbol{F}$ and $\boldsymbol{\sigma}$, respectively, have the following relationships:

$$\boldsymbol{\sigma} = \boldsymbol{\sigma}^{PB} + \boldsymbol{\sigma}^{CB}, \tag{7}$$

$$\boldsymbol{F} = \boldsymbol{F}^{CB} = \boldsymbol{F}^{PB}\boldsymbol{F}^{VP}, \tag{8}$$

where $\boldsymbol{F}^{CB}$ is the deformation gradient for the CB spring. The constitutive equation for the PB spring is given by

$$\boldsymbol{\sigma}^{PB} = \frac{1}{3}C_R^{PB}\sqrt{N^{PB}}\,\frac{\boldsymbol{A}^{PB} - \lambda_c^{PB}\boldsymbol{I}}{\lambda_c^{PB}}\mathcal{L}^{-1}\left(\frac{\lambda_c^{PB}}{\sqrt{N^{PB}}}\right) + p^{PB}\boldsymbol{I}, \tag{9}$$

where quantities with superscript "*PB*" are those for the PB chain.

Similar to Eq. (6), the rubber elastic modulus C_R^{PB} and the limit stretch $\sqrt{N^{PB}}$ in Eq. (9) are functions of the density of PB chain n^{PB}. Because the chain density is proportional to the density of the bonding, the mechanical response of the PB spring changes with the separation and recombination of the PB. Therefore, the macroscopic mechanical property can be controlled by degrees of separation and recombination of the PB during deformation. In the present study, the rates are defined as functions of the current density of the PB, stress, and strain rate. The separation rate is assumed to increase when the current PB n^{PB} and the equivalent stress of the PB chain σ_{eq}^{PB} are large. The function of the elastic and inelastic stretches, $\psi\left(\lambda^{PB}, \lambda^{VP}\right)$, which is explained later, is also introduced to control the development of the residual strain in the cyclic test. On the other hand, the recombination rate increase with a decrease in the density of the PB. Moreover, we introduce the strain rate dependency of the separation and recombination by adding the equivalent strain rate $\dot{\bar{\varepsilon}}$ with strain rate sensitivity m. The rates of separation and recombination, $\dot{r}^{(-)}$ and $\dot{r}^{(+)}$, respectively, are given by

$$\dot{r}^{(-)} = \dot{r}_0^{(-)}\frac{n^{PB} - n_\infty^{PB}}{n_0^{PB} - n_\infty^{PB}}\left(\frac{\sigma_{eq}^{PB}}{aC_R^{PB}}\right)^{\alpha}\left(\frac{\dot{\varepsilon}}{\dot{\varepsilon}_0}\right)^{m}\psi\left(\lambda^{PB}, \lambda^{VP}\right) \tag{10}$$

$$\dot{r}^{(+)} = \dot{r}_0^{(+)}\frac{n_0^{PB} - n^{PB}}{n_0^{PB} - n_\infty^{PB}}\left(\frac{\dot{\varepsilon}}{\dot{\varepsilon}_0}\right)^{m}, \tag{11}$$

where $\dot{r}_0^{(-)}$ and $\dot{r}_0^{(+)}$ are the coefficients of the separation and recombination rates, respectively; n_0^{PB} and n_∞^{PB} are the initial and final densities of the PB chain for given temperature, respectively; a is the strength coefficient of the PB; α is the stress sensitivity; and $\dot{\varepsilon}_0$ is the reference strain rate.

$\psi\left(\lambda^{PB}, \lambda^{VP}\right)$ controls the separation in unloading and reloading process. This suppresses the separation when the polymer deforms within the already experienced reversible strain range, and characterize the development of the residual strain for a cyclic loading. A comparison of the current and maximum stretches from the unloaded configuration is employed for this term, as

$$\begin{cases} \psi\left(\lambda^{PB},\lambda^{VP}\right)=1 & \text{for} \quad 1\le\dfrac{\lambda-\lambda^{VP}}{\lambda_{\max}-\lambda^{VP}} \\ \psi\left(\lambda^{PB},\lambda^{VP}\right)=\left(\dfrac{\lambda-\lambda^{VP}}{\lambda_{\max}-\lambda^{VP}}\right)^{\beta}=\left(\dfrac{\lambda^{PB}-1}{\lambda_{\max}/\lambda^{VP}-1}\right)^{\beta} & \text{for} \quad 0\le\dfrac{\lambda-\lambda^{VP}}{\lambda_{\max}-\lambda^{VP}}\le 1 \\ \psi\left(\lambda^{PB},\lambda^{VP}\right)=0 & \text{for} \quad \dfrac{\lambda-\lambda^{VP}}{\lambda_{\max}-\lambda^{VP}}\le 0 \end{cases} \tag{12}$$

where $\lambda_{\max}$ is the experienced maximum stretch, $\beta \gg 1$ is the sensitivity for the experienced reversible stretch. When λ is smaller than $\lambda_{\max}$, $\psi\left(\lambda^{PB},\lambda^{VP}\right)$ rapidly decreases from 1. To represent the restart of the separation for loading in inverse direction, the second equation in Eq. (12) is modified as

$$\psi\left(\lambda^{PB},\lambda^{VP}\right)=\left\{\frac{\lambda^{PB}-1}{\lambda_{\max}/\left(\left|\lambda^{VP}-\lambda^{VP}_{\max}\right|+\lambda^{VP}_{\max}\right)-1}\right\}^{\beta}, \tag{13}$$

where $\lambda^{VP}_{\max}$ is the inelastic stretch obtained when the polymer experienced a maximum stretch.

The total rate of change in the PB, $\dot{n}^{PB}$, is obtained using $\dot{r}^{(-)}$ and $\dot{r}^{(+)}$ as

$$\dot{n}^{PB}=n_0^{PB}\left(-\dot{r}^{(-)}+\dot{r}^{(+)}\right) \tag{14}$$

Because C_R^{PB} and N^{PB} are proportional and inversely proportional to chain density n^{PB}, we obtain

$$\frac{\dot{C}_R^{PB}}{C_R^{PB}}=\frac{\dot{n}^{PB}}{n^{PB}}, \tag{15}$$

$$\frac{\dot{N}^{PB}}{N^{PB}}=-\frac{\dot{n}^{PB}}{n^{PB}}, \tag{16}$$

Equations (15) and (16) can reproduce the changes in the stiffness and stretch limit from initial values C_{R0}^{PB} and N_0^{PB} owing to the separation and recombination of the PB during deformation.

Next, we discuss the inelastic flow rule for the polymer. As demonstrated by the experimental results, the thermosetting polymer shows a residual strain even in a very small strain range. Since the yielding function generally employed in representation of the inelastic deformation of metal is not introduced in this model, the inelastic flow causes from the small strain range owing to the change in the polymer network. In this study, we assumed that the inelastic flow reduced the reversible deformation of the PB-chain. In other words, the inelastic flow is caused by the approaching of the current inelastic deformation $\boldsymbol{F}^{VP}$ to the total deformation $\boldsymbol{F}$, as shown in Fig. 8. The inelastic deformation at $t+\Delta t$ is given by

$$\boldsymbol{F}^{VP}\left(t+\Delta t\right)=\Delta\boldsymbol{F}^{VP}\boldsymbol{F}^{VP}=\boldsymbol{F}^{VP}+\dot{\boldsymbol{F}}^{VP}\Delta t, \tag{17}$$

where $\Delta\boldsymbol{F}^{VP}$ and Δt are the infinitesimal increase in the inelastic deformation and time,

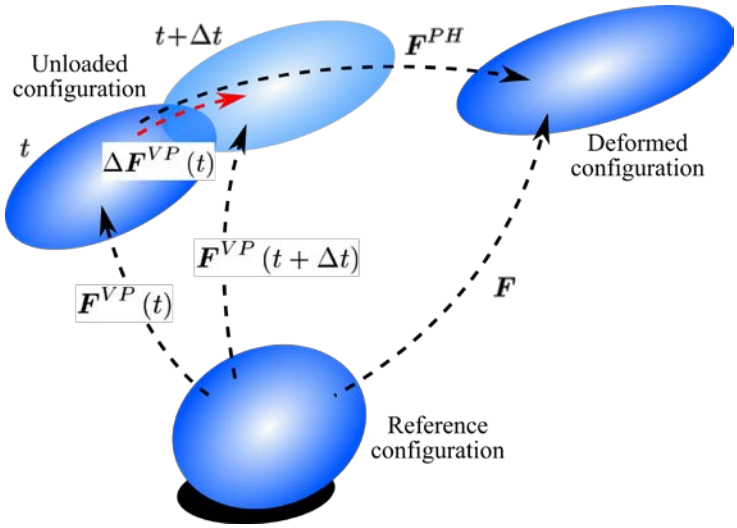

Fig. 8 Schematic illustration of development of inelastic deformation gradient.

respectively. Note that $\Delta \boldsymbol{F}^{VP}$ is observed from the unloaded configuration whereas $\dot{\boldsymbol{F}}^{VP}$ is observed from the reference configuration. As mentioned, $\Delta \boldsymbol{F}^{VP}$ is caused by the approaching of $\boldsymbol{F}^{VP}$ to $\boldsymbol{F}$. Therefore,

$$\Delta \boldsymbol{F}^{VP} = \Delta\phi \boldsymbol{F}^{PB} + \left(1-\Delta\phi\right)\boldsymbol{I}, \tag{18}$$

where $\Delta\phi$ is a scalar parameter to represent the approaching of $\boldsymbol{F}^{VP}$ to $\boldsymbol{F}$. $\Delta\phi = 0$ and $\Delta\phi = 1$ correspond to $\Delta \boldsymbol{F}^{VP} = \boldsymbol{I}$ (no inelastic deformation) and $\Delta \boldsymbol{F}^{VP} = \boldsymbol{F}^{PB}$ (no elastic deformation), respectively. From Eqs. (17) and (18), we obtain

$$\dot{\boldsymbol{F}}^{VP} = \lim_{\Delta t=0} \frac{\Delta \boldsymbol{F}^{VP}\boldsymbol{F}^{VP} - \boldsymbol{F}^{VP}}{\Delta t} = \dot{\phi}\left(\boldsymbol{F}^{PB} - \boldsymbol{I}\right)\boldsymbol{F}^{VP}, \tag{19}$$

where $\dot{\phi} = \lim_{\Delta t=0}\left(\Delta\phi/\Delta t\right)$ is the magnitude of the approaching rate. In the proposed model, the approach of $\boldsymbol{F}^{VP}$ to $\boldsymbol{F}$ occurs the inelastic flow while the separated PB-chains are recombined. Therefore, the magnitude of the approach is given by using recombination rate $\dot{r}^{(+)}$ with the averaged inelastic flow per recombination b as

$$\dot{\boldsymbol{F}}^{VP} = b\dot{r}^{(+)}\left(\boldsymbol{F}^{PB} - \boldsymbol{I}\right)\boldsymbol{F}^{VP}. \tag{20}$$

Eq. (20) contains the inelastic rotation, which enables a description of the inelastic flow-induced anisotropy of the polymer network. On the other hand, an elastic anisotropy, which is induced by the differences in the potential densities in different directions is not introduced in the current model.

3.3 Rate-form large-deformation constitutive equation

Based on the mechanical model proposed in the previous section, a rate-form large-deformation constitutive equation is formulated based on the updated Lagrangian method. First, the deformation gradient rates for the global, PB-chain, and viscoplastic elements are given by

$$\dot{\boldsymbol{F}} = \boldsymbol{L}\boldsymbol{F}\,, \tag{21}$$

$$\dot{\boldsymbol{F}}^{PB} = \boldsymbol{L}^{PB}\boldsymbol{F}^{PB}\,, \tag{22}$$

$$\dot{\boldsymbol{F}}^{VP} = \boldsymbol{L}^{VP}\boldsymbol{F}^{VP}\,, \tag{23}$$

where $\boldsymbol{L}$, $\boldsymbol{L}^{PB}$, and $\boldsymbol{L}^{VP}$ are the velocity gradients for the global, PB-spring, and viscoplastic elements, respectively. From Eq. (8), their relationship is given by

$$\boldsymbol{L} = \dot{\boldsymbol{F}}\boldsymbol{F}^{-1} = \left(\dot{\boldsymbol{F}}^{PB}\boldsymbol{F}^{VP} + \boldsymbol{F}^{PB}\dot{\boldsymbol{F}}^{VP}\right)\left(\boldsymbol{F}^{VP}\right)^{-1}\left(\boldsymbol{F}^{PB}\right)^{-1} = \boldsymbol{L}^{PB} + \boldsymbol{F}^{PB}\boldsymbol{L}^{VP}\left(\boldsymbol{F}^{PB}\right)^{-1}. \tag{24}$$

From Eq. (20), $\boldsymbol{L}^{VP}$ can be described by

$$\boldsymbol{L}^{VP} = \dot{\boldsymbol{F}}^{VP}\left(\boldsymbol{F}^{VP}\right)^{-1} = b\dot{r}^{(+)}\left(\boldsymbol{F}^{PB} - \boldsymbol{I}\right) \qquad . \tag{25}$$

Therefore, Eq. (24) is rewritten as

$$\boldsymbol{L} = \boldsymbol{L}^{PB} + \boldsymbol{L}^{VP}\,. \tag{26}$$

The symmetric and antisymmetric parts of the global velocity gradient, $\boldsymbol{d}$ and $\boldsymbol{\omega}$, respectively, are given by

$$\boldsymbol{d} = \frac{1}{2}\left(\boldsymbol{L} + \boldsymbol{L}^{T}\right) = \frac{1}{2}\left\{\boldsymbol{L}^{PB} + \left(\boldsymbol{L}^{PB}\right)^{T}\right\} + \frac{1}{2}\left\{\boldsymbol{L}^{VP} + \left(\boldsymbol{L}^{VP}\right)^{T}\right\} = \boldsymbol{d}^{PB} + \boldsymbol{d}^{VP}\,, \tag{27}$$

$$\boldsymbol{\omega} = \frac{1}{2}\left(\boldsymbol{L} - \boldsymbol{L}^{T}\right) = \frac{1}{2}\left\{\boldsymbol{L}^{PB} - \left(\boldsymbol{L}^{PB}\right)^{T}\right\} + \frac{1}{2}\left\{\boldsymbol{L}^{VP} - \left(\boldsymbol{L}^{VP}\right)^{T}\right\} = \boldsymbol{\omega}^{PB} + \boldsymbol{\omega}^{VP}\,, \tag{28}$$

The Jaumann rates of the Kirchhoff stress for the PB chain on the axes rotating with the chain, $\overset{\nabla}{\boldsymbol{S}}^{PB*}$, and that on the axes rotating with the material, $\overset{\nabla}{\boldsymbol{S}}^{PB}$, are given by

$$\overset{\nabla}{\boldsymbol{S}}^{PB*} = \dot{\boldsymbol{S}}^{PB} - \boldsymbol{\omega}^{PB}\boldsymbol{\sigma}^{PB} + \boldsymbol{\sigma}^{PB}\boldsymbol{\omega}^{PB}\,, \tag{29}$$

$$\overset{\nabla}{\boldsymbol{S}}^{PB} = \dot{\boldsymbol{S}}^{PB} - \boldsymbol{\omega}\boldsymbol{\sigma}^{PB} + \boldsymbol{\sigma}^{PB}\boldsymbol{\omega}\,, \tag{30}$$

where $\dot{\boldsymbol{S}}^{PB}$ is the material rate of the Kirchhoff stress for the PB spring. The Cauchy stress rate is given by the time differential of Eq. (9) as

$$\dot{\boldsymbol{\sigma}}^{PB} = \frac{1}{3}C_R^{PB}\sqrt{N^{PB}}\left[\left(\frac{\zeta^{PB}}{\sqrt{N^{PB}}} - \frac{\beta^{PB}}{\lambda_c^{PB}}\right)\frac{\left(\boldsymbol{A}^{PB} - \lambda_c^{PB}\boldsymbol{I}\right)\otimes\boldsymbol{A}^{PB}}{\mathrm{tr}\boldsymbol{A}^{PB}} : \boldsymbol{d}^{PB} + \frac{\beta^{PB}}{\lambda_c^{PB}}\left\{\boldsymbol{L}^{PB}\boldsymbol{A}^{PB} + \boldsymbol{A}^{PB}\left(\boldsymbol{L}^{PB}\right)\right\}^{T}\right]$$
$$+ \frac{1}{2}\boldsymbol{\sigma}^{PB}\frac{\dot{n}^{PB}}{n^{PB}}\left(1 + \frac{\zeta^{PB}}{\beta^{PB}}\frac{\lambda_c^{PB}}{\sqrt{N^{PB}}}\right) + \dot{p}^{PB}\boldsymbol{I} \tag{31}$$

where $\beta^{PB} = \mathcal{L}^{-1}\left(\lambda_c^{PB}/\sqrt{N^{PB}}\right)$, $\zeta^{PB} = d\mathcal{L}^{-1}(x)/dx\big|_{x=\lambda_c^{PB}/\sqrt{N^{PB}}} = \beta^{PB2}\Big/\left(1 - \beta^{PB2}\,\mathrm{csch}\,\beta^{PB}\right)$, and the following relationships are used to formulate Eq. (31):

$$\dot{\boldsymbol{A}}^{PB} = \boldsymbol{L}^{PB}\boldsymbol{A}^{PB} + \boldsymbol{A}^{PB}\left(\boldsymbol{L}^{PB}\right)^{T},$$

$$\dot{\lambda}_c^{PB} = \frac{\boldsymbol{A}^{PB} : \boldsymbol{d}^{PB}}{\mathrm{tr}\boldsymbol{A}^{PB}}.$$

Thus, the Jaumann rate of the Cauchy stress for the PB spring on the axes rotating with the chain, $\overset{\nabla}{\boldsymbol{\sigma}}^{PB*}$, is given by

$$\overset{\nabla}{\boldsymbol{\sigma}}^{PB*} = \dot{\boldsymbol{\sigma}}^{PB} - \boldsymbol{\omega}^{PB}\boldsymbol{\sigma}^{PB} + \boldsymbol{\sigma}^{PB}\boldsymbol{\omega}^{PB} = \boldsymbol{D}^{PB} : \boldsymbol{d}^{PB} + \boldsymbol{q}^{PB} \tag{32}$$

where

$$\boldsymbol{D}^{PB} = \frac{1}{3} C_R^{PB} \sqrt{N^{PB}} \left[\left(\frac{\zeta^{PB}}{\sqrt{N^{PB}}} - \frac{\beta^{PB}}{\lambda_c^{PB}} \right) \frac{\left(\boldsymbol{A}^{PB} - \lambda_c^{PB} \boldsymbol{I} \right) \otimes \boldsymbol{A}^{PB}}{\mathrm{tr}\boldsymbol{A}^{PB}} + \frac{\beta^{PB}}{\lambda_c^{PB}} \boldsymbol{H}^{PB} \right] + \psi^{PB} \boldsymbol{I} \otimes \boldsymbol{I},$$

$$\boldsymbol{H} = \left(\delta_{ik} A_{jl}^{PB} + \delta_{il} A_{jk}^{PB} \right) \boldsymbol{e}_i \otimes \boldsymbol{e}_j \otimes \boldsymbol{e}_k \otimes \boldsymbol{e}_l,$$

$$\boldsymbol{q}^{PB} = \frac{1}{2} \boldsymbol{\sigma}^{PB} \frac{\dot{n}^{PB}}{n^{PB}} \left(1 + \frac{\zeta^{PB}}{\beta^{PB}} \frac{\lambda_c^{PB}}{\sqrt{N^{PB}}} \right),$$

and ψ^{PB} is the energy-elastic bulk modulus. Here, we replaced $\overset{\nabla}{\boldsymbol{\sigma}}^{PB*}$ with $\overset{\nabla}{\boldsymbol{S}}^{PB*}$ by assuming that the volume change rate of the PB spring is relatively small. From Eqs. (29) to (32), we formulated the constitutive equation for the PB chain as

$$\overset{\nabla}{\boldsymbol{S}}^{PB} = \boldsymbol{D}^{PB} : \boldsymbol{d} - \boldsymbol{P}^{PB}, \tag{33}$$

where

$$\boldsymbol{P}^{PB} = \boldsymbol{D}^{PB} : \boldsymbol{d}^{VP} + \boldsymbol{\omega}^{VP}\boldsymbol{\sigma}^{PB} - \boldsymbol{\sigma}^{PB}\boldsymbol{\omega}^{VP} - \boldsymbol{q}^{PB}.$$

The constitutive equation for the CB chain is given by

$$\overset{\nabla}{\boldsymbol{S}}^{CB} = \boldsymbol{D}^{CB} : \boldsymbol{d}, \tag{34}$$

where

$$\boldsymbol{D}^{CB} = \frac{1}{3} C_R^{CB} \sqrt{N^{CB}} \left[\left(\frac{\zeta}{\sqrt{N^{CB}}} - \frac{\beta}{\lambda_c^{CB}} \right) \frac{\left(\boldsymbol{A}^{CB} - \lambda_c^{CB} \boldsymbol{I} \right) \otimes \boldsymbol{A}^{CB}}{\mathrm{tr}\boldsymbol{A}^{CB}} + \frac{\beta}{\lambda_c^{CB}} \boldsymbol{H}^{CB} \right] + \psi^{CB} \boldsymbol{I} \otimes \boldsymbol{I}.$$

Finally, the rate-form global constitutive equation is given by

$$\overset{\nabla}{\boldsymbol{S}} = \overset{\nabla}{\boldsymbol{S}}^{PB} + \overset{\nabla}{\boldsymbol{S}}^{CB} = \left(\boldsymbol{D}^{PB} + \boldsymbol{D}^{CB} \right) : \boldsymbol{d} - \boldsymbol{P}^{PB}. \tag{35}$$

The elasto-viscoplastic deformation of the thermosetting polymer can be numerically predicted using the constitutive equation (35).

4 Results

Numerical simulations of monotonic and cyclic tensile tests were performed using the

proposed model. The macroscopic response under uniform deformation can be obtained by directly solving the rate-form constitutive equation (35) under the uniaxial stress states. The material parameters used in the mechanical model representing the responses of both the monotonic and cyclic tests were explored by comparing the computational and experimental results.

The parameters employed in the model are listed in Table 1. Note that the stress-strain relationship for a larger strain range of the employed epoxy specimen could not be obtained, because the obvious necking followed by fracture occurred after the macroscopic yielding. Therefore, the parameters characterizing the stress-strain curve in a larger strain range, e.g., C_R^{CB} and N^{CB}, are not discussed in this manuscript. They should be rechecked after we obtain the experimental data for larger strain range from additional tests under a lower strain rate and/or higher temperature.

Table 1 Material constants employed in model

C_{R0}^{PB}	Initial rubber elasticity for PB spring	520 MPa
C_R^{CB}	Rubber elasticity for CB spring	10 MPa
N_0^{PB}	Initial segment number for PB chain	1.5
N^{CB}	Segment number for CB chain	10
$\dot{r}_0^{(-)}$	Coefficient of separation rate of PB chain	1.55 /s
$\dot{r}_0^{(+)}$	Coefficient of recombination rate of PB chain	0.39 /s
n_∞^{PB}/n_0^{PB}	Ratio of final and initial densities of PB chain	0.25
a	Strength coefficient of PB	0.065
α	Stress sensitivity for separation of PB chain	1.0
$\dot{\varepsilon}_0$	Reference strain rate	1.0 /s
m	Strain rate sensitivity for change in density of PB chain	0.76
β	Experienced reversible stretch sensitivity	35
b	Coefficient of viscoplastic deformation	10.0
ψ^{PB}	Stiffness to volume change for PB chain	3500 MPa
ψ^{CB}	Stiffness to volume change for CB chain	10000 MPa

Fig. 9 shows the computational and experimental results of relationships between the obtained true stress and strain. The proposed model can represent the characteristic deformation behavior of the polymeric material, e.g., the linear response in the initial stage, decrease in the rigidity with increasing strain, gradual transition from elastic to inelastic deformation, strain softening behavior after the macroscopic yielding stress, hardening in the large strain range, and increase in the macroscopic yielding and flow stresses with an increasing strain rate. Although the computational responses do not completely coincide with the experimental results, the important features of the nonlinear response of the polymer can be captured by controlling the development of the PB density.

Fig. 10 shows the computational results of responses to the cyclic tensile tests with different upper stresses and nominal strain rates. The residual strain accumulated during the cyclic test can be

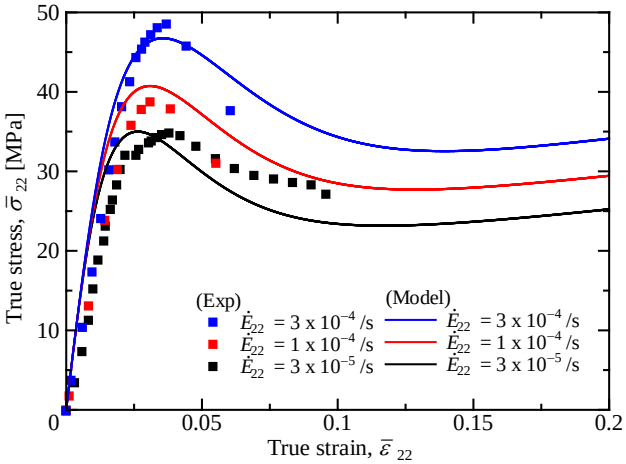

Fig. 9 Comparison of experimental and computational results of relationships between true stress and true strain obtained by monotonic tensile tests with different crosshead speeds.

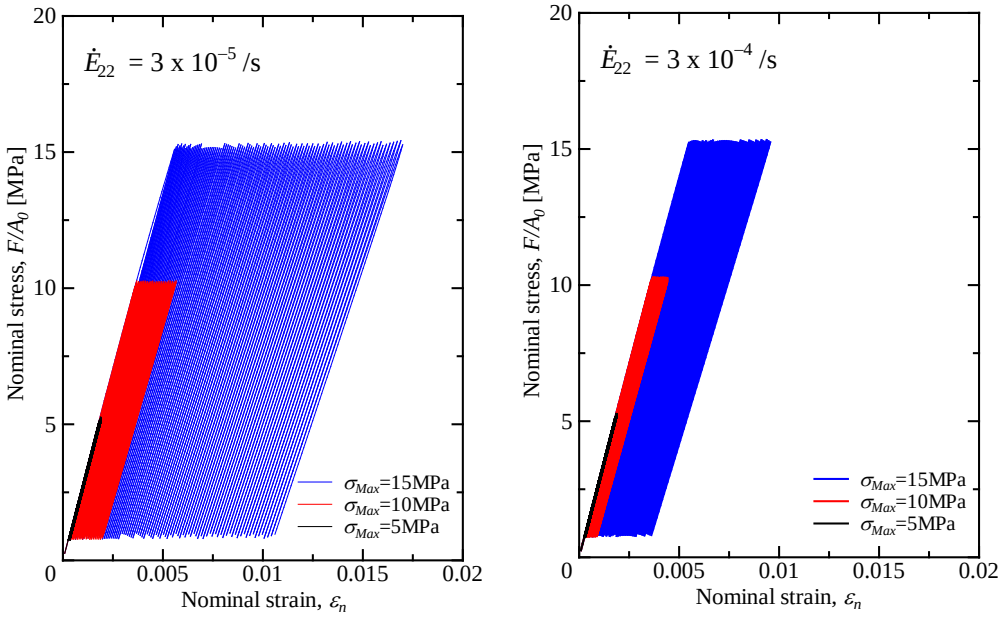

Fig. 10 Computational results of relationships between nominal stress and strain obtained from cyclic tensile tests with different maximum stresses and crosshead speeds.

represented by the proposed model because the nonlinear behavior occurred in a small strain range. Furthermore, the accumulated residual strain increases with increasing upper tensile stress and decreasing strain r ate. To compare the computational and experimental results for the cyclic behavior in further detail, changes in the rigidity and residual strain with an increasing cyclic number are plotted in Figs. 11 and 12. The rigidity decreases with the number of cycles, and the decrease becomes prominent for the cyclic test with a larger upper stress. Furthermore, a comparison of the changes in

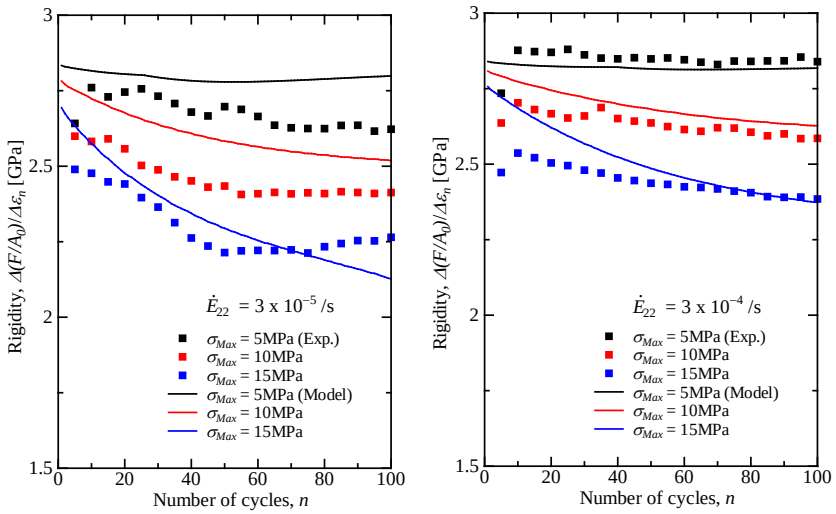

Fig. 11 Comparison of experimental and computational results of change in slope of stress-strain curve for cyclic test.

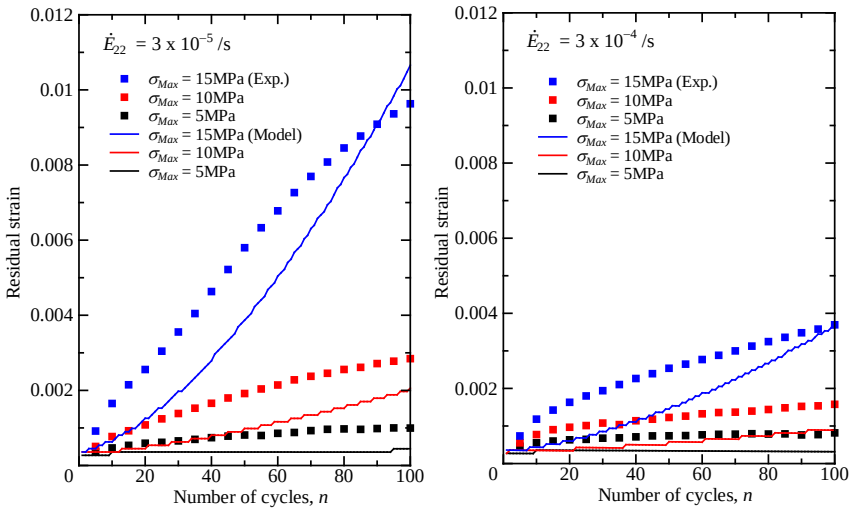

Fig. 12 Comparison of experimental and computational results of change in residual strain for cyclic test.

the rigidity for different strain rates indicates that the decrease in the rigidity becomes gradual during the cyclic test with a larger strain rate. The proposed model can reasonably predict the changes in rigidity with an increasing cyclic number.

The residual strain nonlinearly increases with the cyclic number. A larger residual strain accumulates owing to the larger upper tensile stress and lower strain rate. The proposed model can represent the increase in the residual strain depending on the upper tensile stress and strain rate. However, the residual strain accumulates more rapidly in the earlier cyclic stage in the experimental results than in the computational results. Furthermore, the residual strains for smaller upper tensile stress cases (σ_{Max} = 5 and 10 MPa) are underestimated in the model. These results indicate that the

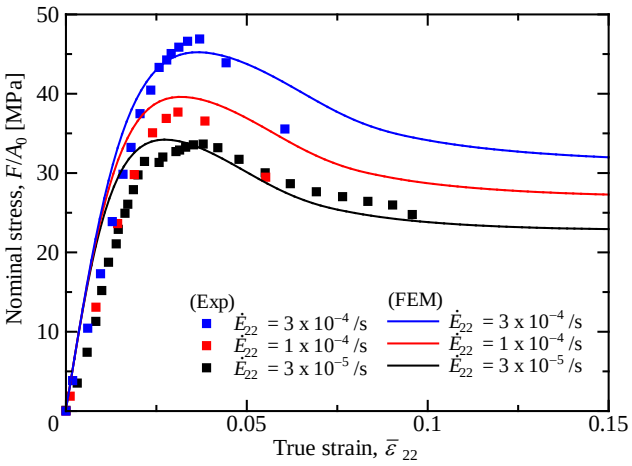

Fig. 13 Comparison of experimental and FEM simulation results of relationships between nominal stress and true strain.

viscoplastic strain causes a much smaller strain range than the proposed model. Further modification of the model is required to improve the prediction of the development of the viscoplastic strain in the cyclic test.

FEM simulations of the monotonic uniaxial tensile tests of the epoxy specimen shown in Fig. 1 were performed using the proposed model with the material parameters listed in Table 1. The quarter area of the specimen without a holding area was meshed using a second-order triangle element with six nodes, and a uniaxial tension with different nominal strain rates $\dot{E}_{22}$ was applied under a two-dimensional plane stress condition. The obtained mechanical responses are shown in Fig. 13. The vertical axis of the figure is the nominal stress, whereas the horizontal axis is the volume-averaged true strain, which is evaluated in the gage section as similar to the experiment.

The obtained response almost coincides with those obtained by the direct solving of the equation under the uniaxial condition in Fig. 9. After the nominal stress decreases, the deformation progresses under an almost constant nominal stress. The rapid drop in stress (as observed in the experimental result) does not occur in the computational result, because the criterion of the fracture of the material is not introduced in the model. In the computational results, the resistance to deformation increases owing to the stretching of the CB spring. The earlier fracture of the specimen in the experiment indicates that the stress acting on the molecular chain may be larger than the limit strength of the chemical bond or molecular chain, and the material may be fractured before the molecular chain orients in the stretching direction.

Fig. 14 shows the distribution of the loading directional strain, ε_{22}, and the equivalent strain rate normalized by the macroscopic strain rate, $\dot{\varepsilon}_{eq}/\dot{E}_{22}$, at different degrees of tensile deformation. The maximum and minimum levels of the contour for the distribution of the loading directional strain are the same as those in the experimental results in Fig. 3. The strain distributes uniformly in the gage section in the initial stages of the deformation, while it concentrates in the central region of the specimen in the later stages. As compared to the experimental results, the predicted concentration of

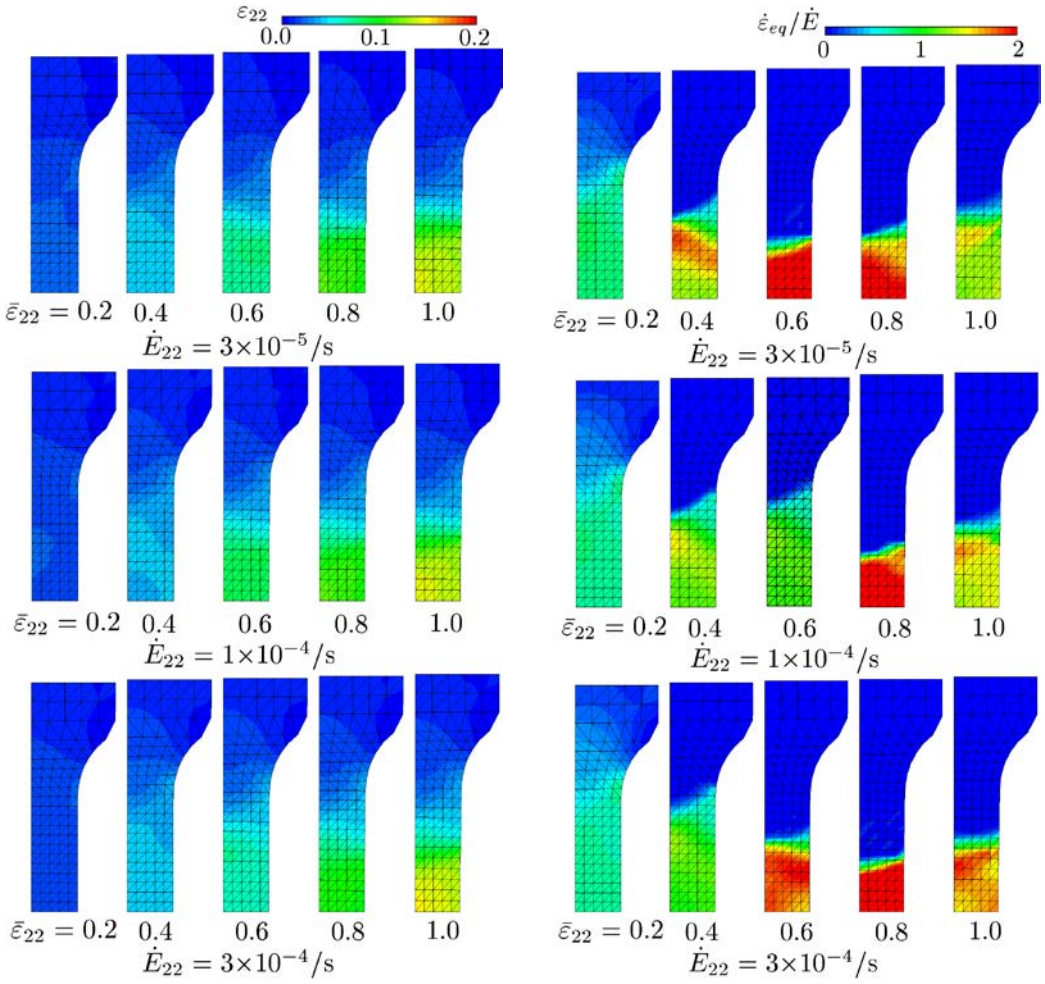

(a) ε_{22} (b) $\dot{\varepsilon}_{eq}/\dot{E}_{22}$

Fig. 14 Distributions of (a) loading directional strain and (b) equivalent strain rate for different degrees of tensile deformation in FEM simulation.

the loading directional strain is less pronounced. In the equivalent strain rate distribution of these deformation stages, the propagation of the currently straining zone from the central to the upper region of the specimen is observed. This propagation of the deformation band occurs owing to the orientation hardening of the molecular chain. Strong strain localization is observed in the experiment because the material fractures before the orientation hardening induce the propagation of the deformation band.

5 Discussion

To represent the nonlinear response of the thermosetting polymer, changes in the mechanical properties owing to the separation and recombination of the PB were introduced in the constitutive equation, based on the molecular chain network theory. The proposed model can represent the

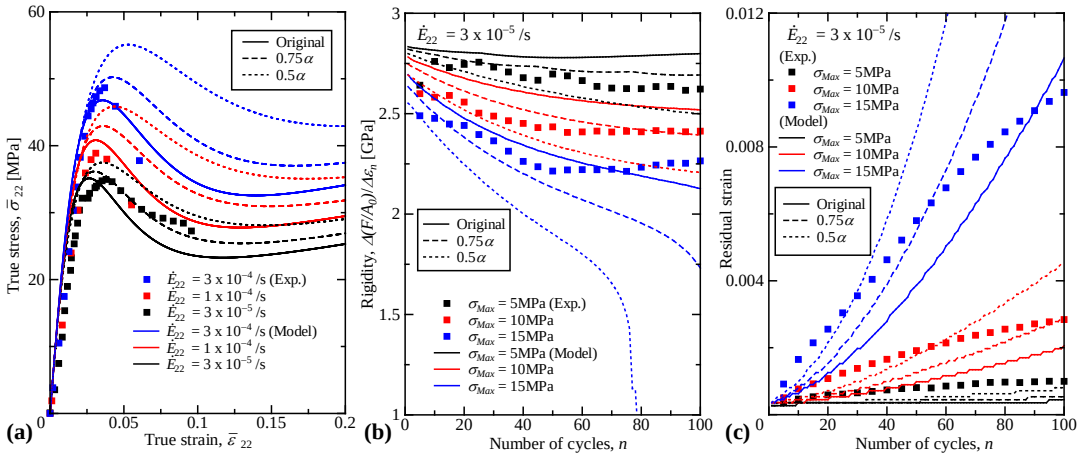

Fig. 15 Effect of stress sensitivity index α on relationships between (a) true stress and strain in monotonic tensile test, and (b) rigidity and (c) residual strain in cyclic tensile test.

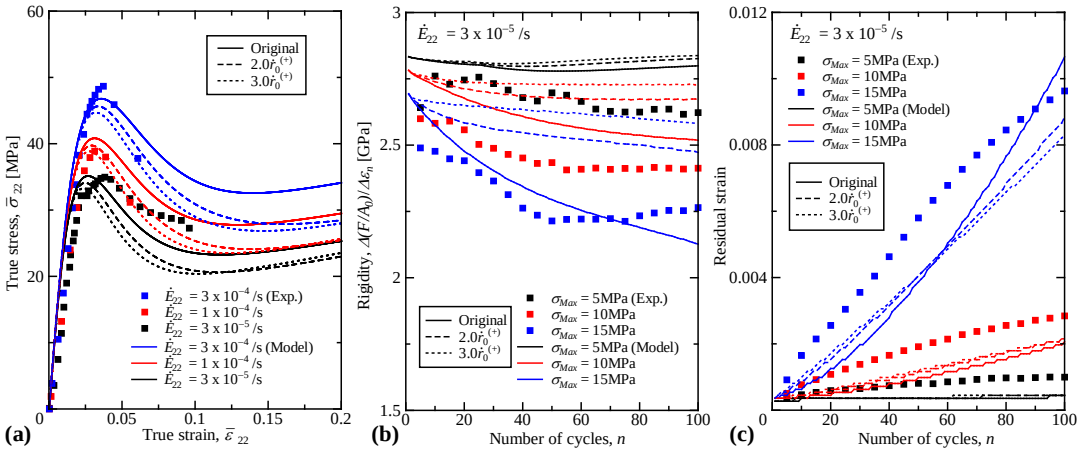

Fig. 16 Effect of recombination rate coefficient $\dot{r}_0^{(+)}$ on relationships between (a) true stress and strain in monotonic tensile test, and (b) rigidity and (c) residual strain in cyclic tensile test.

characteristic nonlinear behavior in the monotonic and cyclic tensile tests. However, the proposed model underestimates the increase in the residual strain in an earlier cyclic stage and the cyclic test with a smaller upper stress. These results indicate that the inelastic strain occurs in a much smaller strain range than the predicted results. A simple way to enlarge the inelastic strain in a smaller strain range is to decrease the macroscopic yielding stress in the model. However, this induces a large difference in the stress-strain relationship under a monotonic tensile test. Alternative ways to improve the accuracy of prediction of the residual strain in the cyclic test in the proposed model are to decrease the stress sensitivity on the separation of the PB and to increase the recombination rate that accompanies the inelastic deformation.

In Fig. 15, the effect of stress sensitivity index α on the monotonic and cyclic tensile tests is investigated. As shown in the stress-strain relation in Fig. 15 (a), the nonlinear response begins in an

earlier strain range with decreasing α. A lower stress sensitivity index causes a more gradual elastic to inelastic transition and suppresses the degree of strain softening. Although this enables an increase in the residual strain without a significant increase in the macroscopic yielding stress, the residual strain in the cyclic test with a larger upper stress also increases, and a decrease in the rigidity becomes prominent.

On the other hand, the effect of the recombination rate coefficient $\dot{r}_0^{(+)}$ is investigated in Fig. 16. With an increase in $\dot{r}_0^{(+)}$, the residual strains in the earlier cyclic stage and the cyclic test with a smaller upper stress become larger. However, the decrease in the rigidity of the material is quite suppressed because the recombination of the PB induces the immediate recovery of the decreased rigidity. These results indicate that the simultaneous development of the rigidity and residual strain agreeing with the experimental results is difficult to accomplish using the present model. A modification of the representation of the inelastic deformation in the smaller strain range is still required.

The important point of this paper is to propose the concept that the characteristic deformation behavior of the polymer (e.g., the nonlinear deformation in the small strain range, gradual elastic-inelastic transition, true softening, and hardening owing to the orientation of the molecular chain) is described by the development of the PB density. Widely employed elastic-inelastic theories converted from those for metal, such as the yielding function and the J_2 flow rule, were not introduced in the proposed model. In the present model, some material parameters are characterized by the microstructure, e.g., the densities of the physical and chemical bonds, and the segment number for a chain, and the rates of separation and recombination are modeled as the functions of the remaining PB, stress, and strain rate. The initial state and the development of these can be investigated by the molecular dynamics simulation and accurate experimental profiling.

On the other hand, the proposed model does not represent the effect of the temperature on the mechanical response of the thermosetting polymer. As mentioned, the deformation resistance decreases when the temperature approaches T_g. Raha and Bowden [38] explained that the decrease in the deformation resistance of the polymer is the result of a decrease in the physical bond density owing to the temperature increase. This idea is employed by indirectly introducing the temperature dependence of the material parameters, e.g., the elastic constant and shear strength of the polymer [39]. The proposed model can directly introduce the effect of temperature on the development of the PB. Furthermore, the inhomogeneity of the density of the polymer, e.g., void, craze, and the locally tightened chain segments, may be developed by deformation, and it affects the mechanical property of the material. The effect of such inhomogeneity can be evaluated by the numerical simulation based on the molecular dynamics simulation. The theoretical and experimental investigation of the effect of the temperature and the inhomogeneity for the material will enable the further development of the time-dependent nonlinear model for the thermosetting polymers.

Conclusion

To describe the elastic-inelastic deformation behavior of a thermosetting polymer, a nonlinear mechanical model in which the development of the physical bond was introduced into the molecular chain network theory was proposed. The proposed model was validated by comparing experimental and computational results.

The deformation behavior of the epoxy specimen under monotonic and cyclic tensile tests was evaluated in an experimental study. The stress-strain relationships under the monotonic tensile test showed that the linear deformation in the earlier strain range was followed by a gradual elastic-inelastic transition. The initial slope of the curve and the macroscopic yielding stress increased with the strain rate. Moreover, the specimen fractured immediately after macroscopic yielding. The strain concentration was observed prior to fracture by the digital image correlation method. In the cyclic test, a decrease in the rigidity and increase in the residual strain with increasing cycles were observed even in a small strain range. Such inelastic deformation depended on the strain rate and the upper stress in the cyclic test.

Computational simulations of the monotonic and cyclic tests under the same conditions as the experiments were performed using the proposed elastic-inelastic model for the thermosetting polymer. In the monotonic tensile simulation, the proposed model represented the important features of the nonlinear response of the polymer by controlling the development of the PB density. Furthermore, the proposed model also well reproduced the decrease in the rigidity and accumulation of the residual strain depending on the strain rate and upper stress in the cyclic tensile tests, even in a small strain range. However, there was a slight difference in the development of the accumulation of the residual strain between the experimental and computational results. A modification of the model in the description of the inelastic strain for a much smaller strain range is required to predict the cyclic behavior more accurately.

Acknowledgement

This work was supported by Council for Science, Technology and Innovation(CSTI), Cross-ministerial Strategic Innovation Promotion Program (SIP), “Multiscale Modeling on Damage and Degradation of Thermosetting Polymers”, (Funding agency:JST).

Reference

[1] K. L. Pickering, M. G. Aruan Efendy and T.M. Le, “A review of recent developments in natural fibre composites and their mechanical performance”, *Composites: Part A*, Vol. **83** (2016), pp. 98–112.

[2] G. Mittala, K. Y. Rheea, V. Mišković-Stankovića and D. Huib, “Reinforcements in multi-scale polymer composites: Processing, properties, and applications”, *Composites: Part B*, Vol. **138** (2018), pp. 122–139.

[3] J. Karger-Kocsis, H. Mahmood and A. Pegoretti, “Recent advances in fiber/matrix interphase

engineering for polymer composites", *Progress in Materials Science*, Vol. **73** (2015), pp. 1–43.

[4] S. Mortazavian and A. Fatemi, "Effects of fiber orientation and anisotropy on tensile strength and elastic modulus of short fiber reinforced polymer composites", *Composites: Part B*, Vol. **72** (2015), pp. 116–129.

[5] H. D. Espinosa, H-C. Lu, P. D. Zavattieri and S. Dwivedi, "A 3-d finite deformation anisotropic visco-plasticity model for fiber composites", *Journal of Composite Materials*, Vol. **35** (2001), pp. 369-410.

[6] E. Kontou and A. Kallimanis, "Thermo-visco-plastic behaviour of fibre-reinforced polymer composites", *Composites Science and Technology*, Vol. **66** (2006), pp. 1588–1596.

[7] I. Doghri and L. Tinel, "Micromechanical modeling and computation of elasto-plastic materials reinforced with distributed-orientation fibers", *International Journal of Plasticity*, Vol. **21** (2005), pp. 1919–1940.

[8] T. Matsuda, D. Okumura, N. Ohno and M. Kawai, "Three-dimensional microscopic interlaminar analysis of cross-ply laminates based on a homogenization theory", *International Journal of Solids and Structures*, Vol. **44** (2007), pp. 8274–8284.

[9] S. Bapanapalli, and B. N. Nguyen, "Prediction of elastic properties for curved fiber polymer composites", *Polymer Composite*, Vol. **29** (2008), pp. 544-550.

[10] E. M. Arruda and M. C. Boyce, "A three-dimensional constitutive model for the large stretch behavior of rubber elastic materials", *Journal of the Mechanics and Physics of Solids*, Vol. **41** (1993), pp. 389-412.

[11] W. Kuhn and F. Grün, "Beziehungen zwischen elastischen Konstanten und Dehnungsdoppelbrechung hochelastischer Stoffe", *Kolloid-Zeitschrift und Zeitschrift für Polymere*, Vol. **101** (1942), pp. 248-271 (in German).

[12] S. F. Edwards and T. Vilgis, "The effect of entanglements in rubber elasticity", *Polymer*, Vol. **27** (1986), pp. 483–492.

[13] C.P. Buckley, D.C. Jones, "Glass-rubber constitutive model for amorphous polymers near the glass transition", *Polymer*, Vol. **36** (1995), pp. 3301-3312.

[14] N. Billon, "New constitutive modeling for time‐dependent mechanical behavior of polymers close to glass transition: Fundamentals and experimental validation", *Journal of Applied Polymer Science*, Vol. **125** (2012), pp. 4390–4401.

[15] M. C. Boyce, D. M. Parks, A. S. Argon, "Large inelastic deformation of glassy polymers. Part I: Rate dependent constitutive model", *Mechanics of Materials*, Vol. **7** (1988), pp. 15-33.

[16] A. S. Argon, "A Theory for Low-temperature Plastic Deformation of Glassy Polymers", *Philosophical Magazine*, Vol. **28** (1973), pp. 839-865.

[17] O. A. Hasan, M. C. Boyce, X. S. Li, and S. Berko, "An Investigation of the yield and postyield behavior and corresponding structure of poly(methyl methacrylate)", *Journal of Polymer Science: Part B Polymer Physics*, Vol. **31** (1993), pp. 185-197.

[18] O. A. Hasan and M. C. Boyce, "A constitutive model for the nonlinear viscoelastic viscoplastic

behavior of glassy polymer", An Investigation of the yield and postyield behavior and corresponding structure of poly(methyl methacrylate)", *Polymer Engineering and Science*, Vol. **35** (1995), pp. 331-344.

[19] Y. Tomita, M. Uchida, "Characterization of micro-to macroscopic deformation behavior of amorphous polymer with heterogeneous distribution of microstructures", *International Journal of Mechanical Sciences*, Vol. **45** (2003), pp. 1703–1716.

[20] L. Anand, N. M. Ames, V. Srivastava and S. A. Chester, "A thermo-mechanically coupled theory for large deformations of amorphous polymers. Part I: Formulation", *International Journal of Plasticity*, Vol. **25** (2009), pp. 1474–1494.

[21] V. Srivastava, S. A. Chester, N. M. Ames and L. Anand, "A thermo-mechanically-coupled large-deformation theory for amorphous polymers in a temperature range which spans their glass transition", *International Journal of Plasticity*, Vol. **26** (2010), pp. 1138–1182

[22] J. L. Bouvard, D. K. Francis, M. A. Tschopp, E. B. Marin, D. J. Bammann and M. F. Horstemeyer, "An internal state variable material model for predicting the time, thermomechanical, and stress state dependence of amorphous glassy polymers under large deformation", *International Journal of Plasticity*, Vol. **42** (2013), pp. 168–193.

[23] F. Gehring, J.-L. Bouvard, and N. Billon, "Modeling of time dependent mechanical behavior of polymers: Comparison between amorphous and semicrystalline polyethylene terephthalate", *Journal of Applied Polymer Science*, Vol. **133** (2016), pp. 1–17.

[24] D. M. Parks and S. Ahzi, "Polycrystalline plastic deformation and texture evolution for crystals lacking five independent slip systems", *Journal of Mechanics and Physics of Solids*, Vol. **38** (1990), pp. 701-724.

[25] B. J. Lee, D. M. Parks, and S. Ahzi, "Micromechanical modeling of large plastic deformation and texture evolution in semi-crystalline polymers", *Journal of Mechanics and Physics and Solids*, Vol. **41** (1993), pp. 1651-1687.

[26] J. A. W. van Dommelen, D. M. Parks, M. C. Boyce, W. A. M. Brekelmans and F. P. T. Baaijens, "Micromechanical modeling of intraspherulitic deformation of semicrystalline polymers", *Polymer*, Vol. **44** (2003), pp. 6089–6101.

[27] M. Uchida and N. Tada, "Micro-, meso- to macroscopic modeling of deformation behavior of semi-crystalline polymer", *International Journal of Plasticity*, Vol. **49** (2013), pp. 164–184.

[28] M. Uchida and N. Tada, "Sequential evaluation of continuous deformation field of semi-crystalline polymers during tensile deformation accompanied by neck propagation", *International Journal of Plasticity*, Vol. **27** (2011), pp. 2085–2102.

[29] S. Yamini and R. J. Young, "The mechanical properties of epoxy resins, Part 1 Mechanisms of plastic deformation", *Journal of Materials Science*, Vol. **15** (1980), pp. 1814-1822.

[30] Y. Leterrier and C. G'Sell, "Viscoelastic analysis of a polyurethane thermosetting resin under relaxation and at constant compression strain rate", *Journal of Materials Science*, Vol. **23** (1988), pp. 4209-4216.

[31] C. Kanchanomai, S. Rattananon and M. Soni, “Effects of loading rate on fracture behavior and mechanism of thermoset epoxy resin”, *Polymer Testing*, Vol. **24** (2005), pp. 886–892.

[32] X. Shen, Z. Xia and F. Ellyin, “Cyclic deformation behavior of an epoxy polymer. Part I: Experimental investigation”, *Polymer Engineering and Science*, Vol. **44** (2004), pp. 2240-2246.

[33] G. Ayoub, F. Zaïri, M. Naït-Abdelaziz and J. M. Gloaguen, “Modelling large deformation behaviour under loading–unloading of semicrystalline polymers: Application to a high density polyethylene”, *International Journal of Plasticity*, Vol. **26** (2010), pp. 329–347.

[34] M. Zrida, H. Laurent, G. Rio, S. Pimbert, V. Grolleau, N. Masmoudi and C. Bradai, “Experimental and numerical study of polypropylene behavior using an hyper-visco-hysteresis constitutive law”, *Computational Materials Science*, Vol. **45** (2009), pp. 516–527.

[35] C. Yu, G. Kang, K. Chen and F. Lu, “A thermo-mechanically coupled nonlinear viscoelastic–viscoplastic cyclic constitutive model for polymeric materials”, *Mechanics of Materials*, Vol. **105** (2017), pp. 1–15.

[36] Z. Xia, X. Shen and Fernand Ellyin, “Cyclic Deformation Behavior of an Epoxy Polymer. Part II: Predictions of Viscoelastic Constitutive Models”, *Polymer Engineering and Science*, Vol. **45** (2005), pp. 103-113.

[37] M. Doi and S. F. Edwards, “Dynamics of concentrated polymer systems. Part 1.—Brownian motion in the equilibrium state”, *Journal of the Chemical Society, Faraday Transactions 2: Molecular and Chemical Physics*, Vol. **74** (1978), pp. 1789-1801.

[38] S. Raha and P. B. Bowden, “Birefringence of plastically deformed poly(methyl methacrylate)”, *Polymer*, Vol. **13** (1972), pp. 174-183.

[39] E. M. Arruda, M. C. Boyce, R. Jayachandran, “Effects of strain rate, temperature and thermomechanical coupling on the finite strain deformation of glassy polymers”, *Mechanics of Materials*, Vol. **19** (1995), pp. 193-212.